

# Interacting topological edge channels

Jonas Strunz<sup>1,2,5\*</sup>, Jonas Wiedenmann<sup>1,2,5</sup>, Christoph Fleckenstein<sup>3,5</sup>, Lukas Lunczer<sup>1,2</sup>, Wouter Beugeling<sup>1,2</sup>, Valentin L. Müller<sup>1,2</sup>, Pragma Shekhar<sup>1,2</sup>, Niccolò Traverso Ziani<sup>3,4</sup>, Saquib Shamim<sup>1,2</sup>, Johannes Kleinlein<sup>1,2</sup>, Hartmut Buhmann<sup>1,2</sup>, Björn Trauzettel<sup>3\*</sup> and Laurens W. Molenkamp<sup>1,2\*</sup>

**Electrical currents in a quantum spin Hall insulator are confined to the boundary of the system. The charge carriers behave as massless relativistic particles whose spin and momentum are coupled to each other. Although the helical character of those states is already established by experiments, there is an open question regarding how those edge states interact with each other when they are brought into close spatial proximity. We employ an inverted HgTe quantum well to guide edge channels from opposite sides of a device into a quasi-one-dimensional constriction. Our transport measurements show that, apart from the expected quantization in integer steps of  $2e^2/h$ , we find an additional plateau at  $e^2/h$ . We combine band structure calculations and repulsive electron–electron interaction effects captured within the Tomonaga–Luttinger liquid model and Rashba spin–orbit coupling to explain our observation in terms of the opening of a spin gap. These results may have direct implications for the study of one-dimensional helical electron quantum optics, and for understanding Majorana and para fermions.**

The discovery of the quantum spin Hall effect<sup>1–3</sup> in HgTe quantum wells<sup>4</sup> was the first landmark in the physics of topological materials. Such quantum wells boast an inverted band structure for well widths  $d_{\text{QW}}$  larger than a critical thickness  $d_c = 6.3$  nm. The quantum spin Hall phase was subsequently also observed in other material systems such as InAs/GaSb double quantum wells<sup>5</sup> and in monolayers of WTe<sub>2</sub> and bismuthene<sup>6,7</sup>. The defining property of this state is the emergence of topologically protected helical edge channels, while the bulk is insulating. Non-local edge transport and spin polarization of these edge channels has already been demonstrated in HgTe quantum wells<sup>8,9</sup>. Here, we investigate the open question of how helical edge states interact with each other.

A quantum point contact (QPC) can be used to guide edge channels from opposite boundaries of the sample into a constriction. Such a device allows for studies of charge and spin transfer mechanisms, for example, by adjusting the overlap of the edge states<sup>10–20</sup>. Besides the general interest in the study of transport processes in such a device, the appropriate model to describe the essential physics and to capture interaction effects of helical edge states is still unclear.

We present the realization of a QPC based on HgTe quantum wells, as evidenced by the observation of the expected conductance steps in integer values of  $G_0$ . Our lithographic process allows the fabrication of sophisticated nanostructures based on topological materials without lowering the material quality. Depending on the QPC width  $W_{\text{QPC}}$  and quantum well thickness  $d_{\text{QW}}$ , we observe a fractional plateau at  $0.5G_0$  in the absence of an applied magnetic field. We label this phenomenon the 0.5 anomaly, in analogy with the 0.7 anomaly frequently observed in QPCs fabricated in more conventional semiconductors<sup>21</sup>. Self-consistent  $\mathbf{k}\cdot\mathbf{p}$  calculations allow us to identify the most plausible transport mechanism. Using the theory of helical Tomonaga–Luttinger liquids, we associate the experimental results with the presence of a spin gap. The bias and temperature dependencies of the 0.5 anomaly are in agreement with

such a gap. Furthermore, we identify an indicator of the conventional 0.7 anomaly in our devices when increasing the applied bias voltage. This observation is in qualitative agreement with our theory and the explanation given for the 0.7 anomaly in ref. <sup>22</sup>.

## Realization of a quantum spin Hall QPC

Figure 1a,b shows a scanning electron micrograph (SEM) image of a HgTe QPC and a schematic of the device. A constriction is formed by wet chemical etching of the HgTe heterostructure<sup>23</sup> and a top-gate electrode is used to tune the chemical potential. The thickness of the HgTe layer, if not explicitly stated otherwise, is  $d_{\text{QW}} = 10.5$  nm. Details about the device fabrication are presented in the Methods and material parameters are provided in Supplementary Section I.

The conductance  $G$  of a representative QPC as a function of applied gate voltage  $V_G$  is depicted in Fig. 1c. Three regimes can be identified. For gate voltages  $V_G \geq -0.75$  V, we observe conventional QPC behaviour. Conductance plateaux develop at integer multiples of  $G_0$  and the quality of quantization can be improved by applying a small magnetic field (shown in red). For gate voltages in the range  $-0.75$  V  $> V_G > -1.2$  V the QPC is in the quantum spin Hall regime. A long plateau around  $G_0$  is assigned to two helical edge channels. For still more negative gate voltages  $V_G \leq -1.2$  V, a step-like transition from  $G_0$  to a long plateau at  $0.5G_0$  is observed. The inset shows the good precision of the quantization even at zero magnetic field.

## The 0.5 anomaly

The anomalous plateau at  $0.5G_0$  is a robust signature as it is stable over multiple thermal cycles and we have reproduced it in several devices. An overview of various devices is presented in Fig. 2. The 0.5 anomaly can be identified in devices numbered II to V, which have a constriction width approximately between 100 and 200 nm (Fig. 2b,c). For wider constrictions, such as that in QPC-I ( $W_{\text{QPC}} \approx 250$  nm, Fig. 2a), the conductance drops below  $G_0$  but does not reach  $0.5G_0$ . This behaviour suggests that an interaction

<sup>1</sup>Experimentelle Physik III, Physikalisches Institut, Universität Würzburg, Würzburg, Germany. <sup>2</sup>Institute for Topological Insulators, Würzburg, Germany.

<sup>3</sup>Institute of Theoretical Physics and Astrophysics, University of Würzburg, Würzburg, Germany. <sup>4</sup>Dipartimento di Fisica, Università di Genova, CNR-SPIN, Genova, Italy. <sup>5</sup>These authors contributed equally: Jonas Strunz, Jonas Wiedenmann, Christoph Fleckenstein. \*e-mail: [jonas.strunz@physik.uni-wuerzburg.de](mailto:jonas.strunz@physik.uni-wuerzburg.de); [trauzettel@physik.uni-wuerzburg.de](mailto:trauzettel@physik.uni-wuerzburg.de); [molenkamp@physik.uni-wuerzburg.de](mailto:molenkamp@physik.uni-wuerzburg.de)

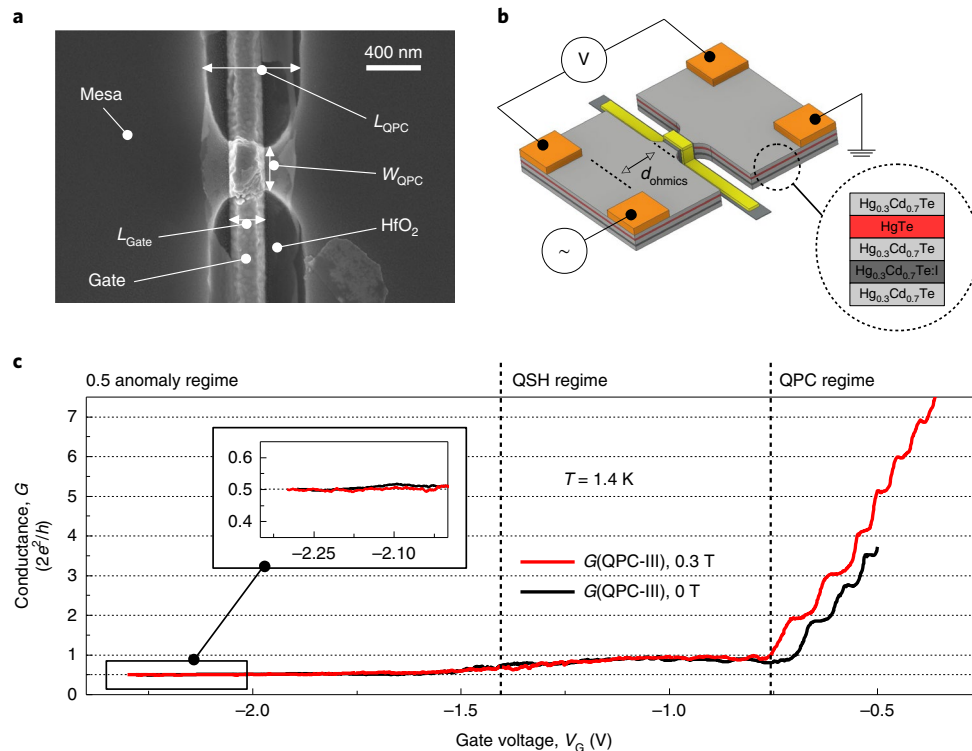


**Fig. 1 | Realization of a topological QPC.** **a**, SEM image of a typical device. A narrow channel is defined in the HgTe mesa with width  $W_{\text{QPC}}$  and length  $L_{\text{QPC}}$ . A metallic gate electrode is separated from the mesa by a  $\text{HfO}_2$  dielectric. **b**, Schematic of the QPC design and measurement set-up. The gate electrode is depicted in yellow and the ohmic contacts in orange. The inset shows the epitaxially grown layer stack on a commercially available  $\text{Cd}_{0.96}\text{Zn}_{0.04}\text{Te}$  substrate. **c**, Gate voltage dependence of the conductance of QPC-III ( $W_{\text{QPC}} \approx 150$  nm) measured at 1.4 K. The conductance is divided into three regimes separated by vertical dashed lines. In the QPC regime, integer steps up to  $14e^2/h$  are observed. The pure quantum spin Hall regime is defined by a conductance of  $2e^2/h$  (indicated as the QSH regime in **c**). In the 0.5 anomaly regime, an interaction-driven gap opens, leading to a quantized conductance of  $e^2/h$ . The inset shows an enlarged view of the 0.5 anomaly regime.

between the edge channels is crucial for the appearance of the 0.5 anomaly. The conductance of  $e^2/h$  implies the transmission of one channel while the other is reflected. We present preliminary data of the detection of this backscattered state in Supplementary Fig. 3. In that experiment, adjacent voltage probes in a Hall geometry next to a QPC were used to detect an emerging voltage drop, with the QPC entering the 0.5 anomaly regime at  $B=0$  T. Our measurement of the transversal resistance  $R_{xy}$  is consistent with predictions by Landauer–Büttiker theory for one reflected helical edge channel.

The conductance in the bulk bandgap vanishes for very narrow QPCs, as depicted in Fig. 2d ( $W_{\text{QPC}} \approx 25$  nm). In this regime, the transport shows a Coulomb blockade behaviour typical for quantum dots (Supplementary Fig. 2). We believe that inter-edge coupling, local disorder or both are responsible for the localization. The suppression of conductance for narrow QPCs sets an experimental upper limit for the wavefunction width of the edge states. Because we are still able to observe a  $G_0$  plateau for  $W_{\text{QPC}} \approx 150$  nm and no suppression of conductance inside the bandgap for  $W_{\text{QPC}} \approx 100$  nm, we conclude that the localization of each edge channel has to be smaller than 50 nm, in agreement with theory<sup>20</sup>. In the QPCs with  $W_{\text{QPC}} \approx 100$  nm, shown in Fig. 2c, a plateau at  $G_0$  is not visible anymore, whereas the one at  $0.5G_0$  can still be observed (to some extent). We attribute this behaviour to stronger inter-edge interactions in narrower QPCs in our model, as described in the section ‘Opening of a spin gap due to Coulomb interactions’.

The 0.5 anomaly is observed at large negative gate voltages over a wide voltage range. The gate efficiency in our devices is known from reference Hall bars to be  $\Delta n_e / \Delta V_G \approx 8\text{--}10 \times 10^{11} \text{ cm}^{-2} \text{ V}^{-1}$ , where  $n_e$  is the electron density. Therefore, we conclude that the

bulk density in the regime of the 0.5 anomaly is strongly p-doped ( $n_h > 1 \times 10^{12} \text{ cm}^{-2}$ ). Bulk transport through the QPC in this regime is suppressed, as will be further discussed in the following. As shown in Fig. 1c, a magnetic field of  $B \lesssim 300$  mT does not influence the 0.5 anomaly.

The QPC conductance of a thinner, but still inverted HgTe quantum well ( $d_{\text{QW}} = 7.0 \text{ nm} > d_c$ ) with  $W_{\text{QPC}} \approx 100$  nm is shown in Fig. 2e. By lowering the gate voltage, conventional conductance steps are first observed. The lowest conductance in this device is around  $G_0$ , indicating the quantum spin Hall regime. We carefully checked that indeed no 0.5 anomaly is observed in thin quantum wells by studying several QPCs with varying  $W_{\text{QPC}}$ , measured in a large temperature (25 mK up to 10 K) and gate voltage range (Fig. 2f). These findings guide us to the importance of the underlying band structure to identify the mechanism for the 0.5 anomaly.

### Band structure calculations

Using  $\mathbf{k} \cdot \mathbf{p}$  theory based on the eight-band Kane model, we first calculated the bulk band structure of an infinitely wide slab of quantum well material (black curves, Fig. 3a–c)<sup>24</sup>. A more elaborated calculation (using a finite width of  $W_{\text{QPC}} = 150$  nm) for the system allows us to gain information about the situation inside the QPC constriction (coloured dots in the plots).

The band structure of a quantum well with  $d_{\text{QW}} = 7$  nm (Fig. 3a) shows the inverted bandgap between the  $|H_{1\pm}\rangle$  and  $|E_{1\pm}\rangle$  sub-bands as conduction and valence band, respectively. Importantly, the crossing point of the edge channels (Dirac point) lies in the bulk bandgap. In contrast, the order of bands in the 10.5 nm wide quantum well is rather different (Fig. 3b). In this

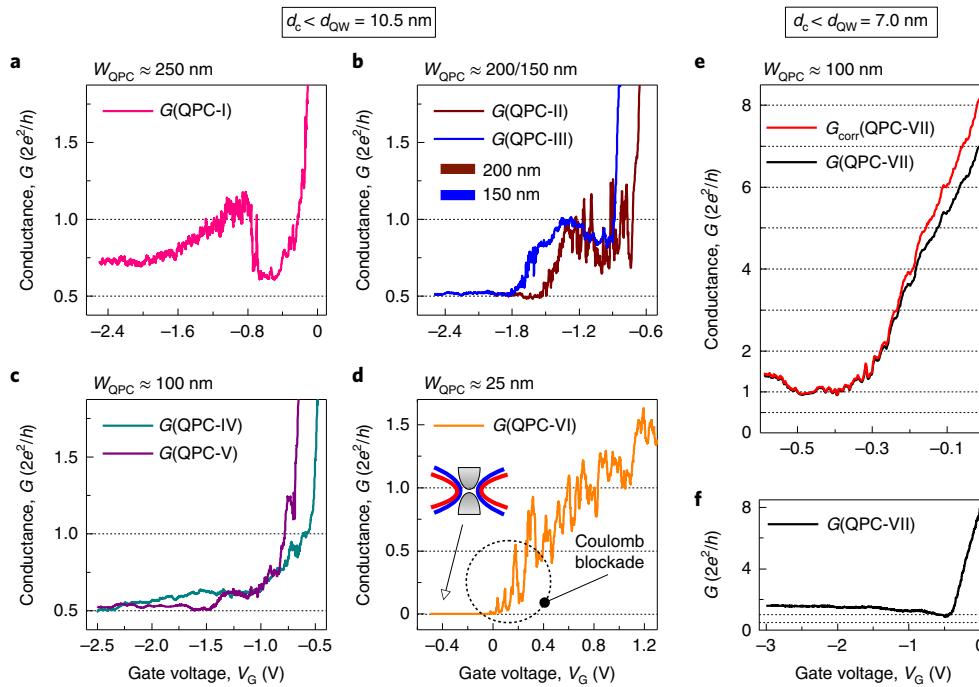


**Fig. 2 | Width dependencies of the 0.5 anomaly.** **a–d**, Conductance as a function of gate voltage  $V_G$  measured at zero magnetic field and a temperature of  $T \approx 1.4$  K for QPCs with varying width  $W_{\text{QPC}}$ : 250 nm (**a**), 200/150 nm (**b**), 100 nm (**c**) and 25 nm (**d**). The blue trace in **b** represents a second sweep of QPC-III. The shift in  $V_G$  compared with the data of Fig. 1c is due to hysteresis effects of the gate dielectric. **e, f**, Conductance of a QPC based on a quantum well width of  $d_{\text{QW}} = 7.0$  nm over a conventional (**e**) (raw data are shown in black, while a serial resistance of  $260 \Omega$  was subtracted for the red trace) and over a wider gate voltage range (**f**).

case, the bandgap is between the first  $|H_{1\pm}\rangle$  and second  $|H_{2\pm}\rangle$  heavy hole sub-band. The  $|E_{1\pm}\rangle$  sub-band—still responsible for the band inversion—lies energetically below the  $|H_{2\pm}\rangle$  state. Then, the Dirac point is buried deeply in the valence band and the edge states hybridize with the bulk states if they spatially overlap<sup>25</sup>. However, at the indicated position of the chemical potential in Fig. 3c (dashed line), the edge states are well localized at the sample edge while the bulk density is already dominated by holes. The corresponding edge wavefunction has a width of  $\sim 10$  nm. This value is in qualitative agreement with our observation of unperturbed edge channel transport for QPC widths  $W_{\text{QPC}} \geq 100$  nm.

The position of the Dirac point in the valence band and the flat heavy hole bands have several implications for carrier transport. First, lowering the gate voltage in wider quantum wells pushes the chemical potential into the heavy hole  $|H_{2\pm}\rangle$  bulk sub-bands, where the valence band structure exhibits a camel back-like shape. As a consequence, the Fermi level is pinned at the flat valence band edge. Second, the large Fermi momentum mismatch between valence and conduction bands suppresses inter-band transitions and thus also suppresses bulk transport in the p regime. In addition, the separation in momentum space between the edge and bulk states allows their coexistence without hybridization. These arguments explain the range in gate voltage of the quantum spin Hall plateau at  $G_0$ , which is longer than the ‘conventional’ steps, as well as the suppression of bulk conductance when entering the valence band. Furthermore, the application of a large negative gate voltage induces a strong Rashba effect. Self-consistent  $\mathbf{k} \cdot \mathbf{p}$  calculations allow us to include the applied electric field, and the resulting band structure is shown in Fig. 3c<sup>24</sup>. The dispersion of the bulk bands shows the typical Rashba splitting, while the dispersion of the edge states is not affected. The Rashba coupling does induce an energy dependence of the spin-momentum locking in the edge states, as indicated by the tilted arrows<sup>26,27</sup>. However, the emergence of a gapless generic

helical spectrum cannot explain a 0.5 anomaly. Hence, we have to take interactions into account.

### Opening of a spin gap due to Coulomb interactions

It is well known that the combination of Rashba spin–orbit coupling and electron–electron interactions at the helical edge can, in principle, give rise to backscattering (Supplementary Section III)<sup>28,29</sup>. When both edge channels interact with each other, a variety of two-particle scattering terms are allowed<sup>12,13,18,30</sup>. In general, however, most of these terms are either not relevant in a renormalization group sense, or do not apply to the constraints set by the band structure in our set-up.

As indicated by the  $\mathbf{k} \cdot \mathbf{p}$  calculations, the inverted quantum wells with  $d = 10.5$  nm have a Fermi wavevector of  $k_F \approx 0.1 \text{ nm}^{-1}$ . Backscattering processes, which do not preserve the number of right- and left-moving edge channels, hence oscillate as a function of space over a scale of  $k_F^{-1}$ . Because the length of the QPC is of the order of  $L \approx 100$  nm, net effects of these terms should average out.

Following those arguments and assuming (weak) repulsive electron–electron interactions, we show in Supplementary Section III that the most relevant two-particle scattering term is

$$H_S = g_S \int_0^L dx [\hat{\chi}_{R,+}^\dagger(x) \hat{\chi}_{L,+}(x) \hat{\chi}_{L,-}^\dagger(x) \hat{\chi}_{R,-}(x) + \text{h.c.}] \quad (1)$$

where  $\hat{\chi}_{\nu,\pm}(x)$ , with  $\nu \in R, L$  being the right- (R) and left- (L) moving Fermi field operators of the upper (+) or lower (–) edge, respectively. Because the spin degree of freedom and the direction of motion are pinned in each helical liquid, we only indicate the direction of motion in equation (1) and drop the spin degree of freedom for ease of notation. Evidently,  $H_S$  describes a backscattering process between the (+) and (–) edges preserving the number of right and left movers (see Fig. 3d for a schematic).

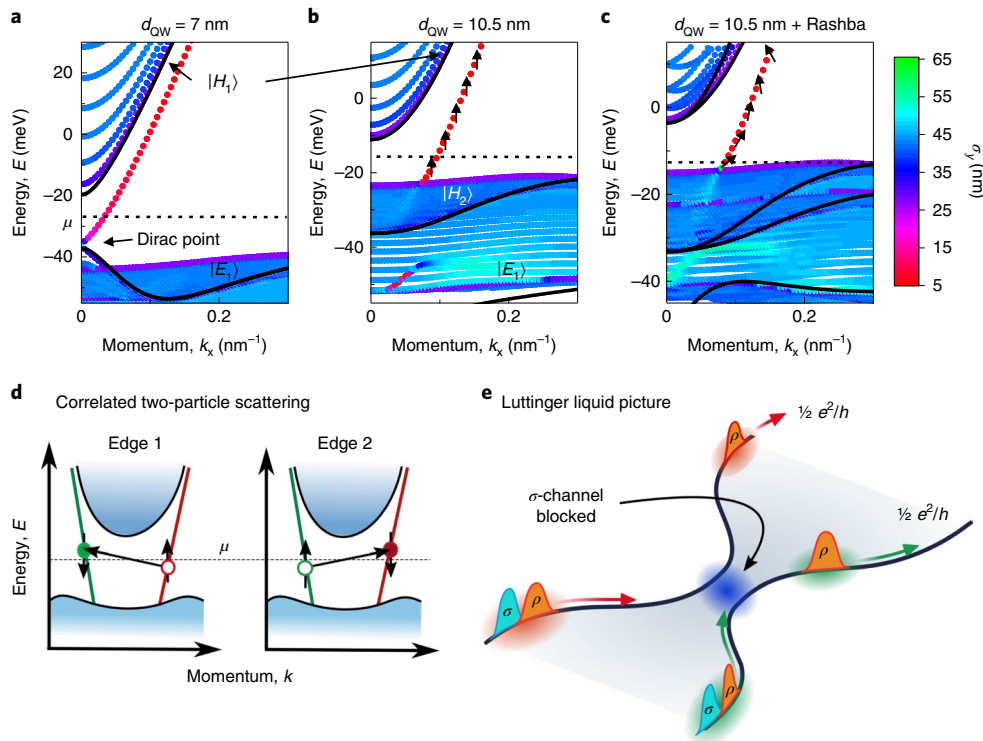


**Fig. 3 |  $k \cdot p$  band structure calculations and illustrations of the scattering process.** **a**, The calculated band structure of a 7.0 nm quantum well. The Dirac point lies in the bulk bandgap. The chemical potential  $\mu$  is depicted by the black dashed line. **b, c**, The band structure for a 10.5-nm-thick quantum well. Realistic finite electric fields have been applied to the quantum well on the bottom (to simulate iodine doping) and on the top (gate electrode) in **c**, which introduces a Rashba effect as well as a tilting of the spin polarization of the helical edge states away from the normal, as sketched by the arrows. Black lines indicate the bulk band structure. The coloured dots are the results of calculations performed on a finite ribbon with a width of 150 nm in the  $y$  direction. The colour key shows the wavefunction standard deviation  $\sigma_y$  in the  $y$  direction. Small values (red) indicate strongly localized states and large values (blue) indicate bulk-like states. **d**, Schematic of the correlated scattering process, responsible for the spin gap. **e**, Illustration of the reduction of conductance in the Tomonaga–Luttinger liquid picture, where  $\sigma$  and  $\rho$  indicate the bosonic charge and spin fields.

In our minimal model, introduced in Supplementary Section III, equation (1) appears due to the combination of Rashba spin–orbit coupling and electron–electron interactions with broken SU(2) symmetry of the spin degree of freedom. The coupling constant

$$g_s = \sin^2(\gamma) \frac{g_{2\perp} - g_{4\perp}}{2} \quad (2)$$

is directly related to the magnitude of the Rashba coupling strength  $\alpha$  via  $\gamma = \arctan(\alpha/(\hbar v_f))$ , as well as to the electron–electron interaction processes across the edges, parametrized by  $g_{2\perp}$  and  $g_{4\perp}$ . In the presence of strong spin–orbit coupling, SU(2) invariance is broken at the single-particle level. Hence, it makes sense that it remains to be broken in the presence of interactions, which implies that  $g_{2\perp} \neq g_{4\perp}$ .

The Fermi level pinning in the samples with quantum well thickness of 10.5 nm hence allows the coupling constant  $g_s$  to grow with increasing electric field and thus Rashba coupling. This indicates the importance of the camel back in the band structure shown in Fig. 3c for the development of a sufficiently large  $g_s$ .

Using bosonization techniques, we can demonstrate that equation (1) acts as a gap to the spin sector<sup>31</sup>. The effective Hamiltonian is

$$H_{\text{eff}} = \frac{1}{2\pi} \int_0^L dx \sum_{\nu=\sigma,\rho} \left[ \frac{u_\nu}{K_\nu} (\partial_x \phi_\nu)^2 + u_\nu K_\nu (\partial_x \theta_\nu)^2 \right] + \tilde{g}_s \cos(2\sqrt{2}\theta_\sigma) \quad (3)$$

where  $\phi_\nu(x)$  and  $\theta_\nu(x)$  ( $\nu \in \rho, \sigma$ ) describe bosonic fields acting on the spin ( $\sigma$ ) and charge sector ( $\rho$ ),  $\tilde{g}_s$  is a rescaled version of  $g_s$ ,  $u_\nu$  represent the normalized velocities and  $K_\nu$  are the Tomonaga–Luttinger interaction parameters ranging between  $0 \leq K_\rho \leq 1$  and  $1 \leq K_\sigma \leq 1/K_\rho$  for a repulsively interacting system. We have dropped the explicit spatial dependence of the bosonic fields for ease of notation. The last term in equation (3)—proportional to  $\tilde{g}_s$ —corresponds to a gap in the  $\sigma$  sector of the otherwise free bosonic theory.

### Experimental consequences of a spin gap

Usually, spin gaps are not detectable in charge transport experiments of purely one-dimensional (1D) systems. However, the strong localization of the single-particle wavefunctions at the edges of the QPC implies that, in the present case, the system is by no means a single 1D system, but has to be treated as two spatially separated 1D systems, coupled by Coulomb interactions.

Thus, we have to use two distinct current operators  $j_\pm(x) \approx \partial_x(\phi_\rho(x) \mp \theta_\sigma(x))$  for the two edges ( $\pm$ ). A voltage bias couples to each helical edge state separately. This assumption leads to a reduced conductance of  $G = 0.5G_0$  in the presence of the spin gap (see also Fig. 3e). In the absence of the spin gap, we instead find  $G = G_0$  (Supplementary Section III).

As is observable in Fig. 2, the fluctuations on top of the 0.5 anomaly plateau are considerably smaller than in the quantum spin Hall regime, where both helical channels are transmitted. In the presence of equation (1), our renormalization group analysis (Supplementary Section III) indeed predicts a reduced sensitivity to impurity back-scattering, consistent with this observation. Moreover, we note that

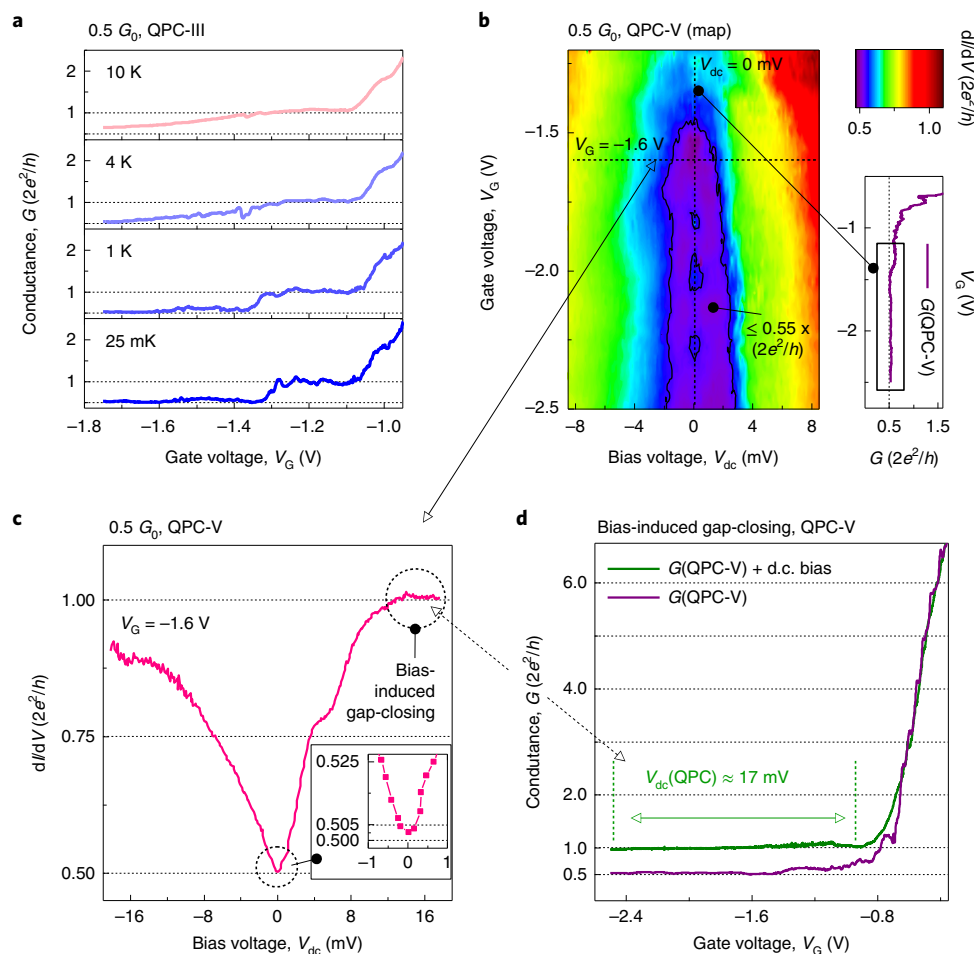


**Fig. 4 | Temperature and d.c. bias dependence of the 0.5 anomaly.** **a**, Temperature dependence of the  $2e^2/h$  to  $e^2/h$  transition of QPC-III. **b**, Differential conductance map of QPC-V as a function of bias and gate voltage. The violet area indicates the regime of the 0.5 anomaly. **c**, Line cut of the bias dependence at  $V_G = -1.6$  V. We attribute the asymmetry of the bias dependence to self-gating effects. **d**, Conductance as a function of gate voltage of QPC-V for zero applied d.c. bias (violet) and a large (green) applied d.c. bias of 17 mV.

the proposed mechanism is not affected by magnetic fields, also consistent with the experiment.

The absence of the 0.5 anomaly in thinner quantum wells can be understood through the lack of Fermi level pinning. In thicker quantum wells (10.5 nm), the application of a strong electric field allows us to generate a sufficiently large Rashba field without substantially affecting the electron density of the edge states. The reason for this is that the camel back of the valence band has a large density of states at the Fermi energy that gives rise to Fermi level pinning (see the horizontal dashed line in Fig. 3c). In contrast, in thinner quantum wells (7 nm), the camel back is far away (in energy) from the Fermi level (see the horizontal dashed line in Fig. 3a). Hence, in that case, we are not able to apply strong electric fields without substantially affecting the electron density of the edge states. We argue that the resulting Rashba field, acting on the edge states in the transport regime with conductance  $2e^2/h$ , is too small to observe the 0.5 anomaly.

The bias and temperature dependence of the conductance, depicted in Fig. 4, helps us to quantify the observed energy scales. As shown in Fig. 4a, the 0.5 anomaly is observable up to temperatures of 1.4 K. For higher temperatures ( $T \geq 4$  K), the quantization is lost and the conductance increases with increasing temperatures. The range 2–4 K as the upper limit to which the quantized plateau is observed sets an energy scale of the spin gap of  $\Delta E \approx 150$ –300 eV. This energy scale is in good agreement with the bias dependence

shown in Fig. 4b. There, the low a.c. bias has been superimposed by a d.c. bias voltage  $V_{dc}$ . The gate voltage regime in which the 0.5 anomaly can be observed opens around  $V_G = -1.6$  V. We are able to observe the 0.5 anomaly up to  $eV_{dc} \approx 200$ –400 eV (Fig. 4c), depending on the gate voltage. A similar estimate can be made for the energy scale set by the length of the QPC,  $\hbar v_F/L_{Gate} \approx 200$ –300  $\mu$ eV (with  $L_{Gate} \approx 200$ –300 nm and  $v_F \approx 1 \times 10^5$  m s $^{-1}$ , estimated from the helical dispersion). The agreement of the magnitudes of all energy and temperature scales is remarkable. We conclude that they set the typical energy scale required for the development of the 0.5 anomaly.

Increasing the applied bias voltage further, the conductance increases beyond the 0.5 anomaly and a second step-like plateau is visible around  $\sim 0.8G_0$  (Fig. 4c). We conjecture that this feature is related to the 0.7 anomaly commonly observed in conventional QPCs. The emergence of this conventional 0.7-like signature is in qualitative agreement with the explanation given in refs.<sup>22,32,33</sup> for GaAs based structures. Depending on the device, we are also sometimes able to identify a 0.7 feature as a function of gate voltage (Fig. 2b). Increasing the bias even further closes the interaction induced gap and the conduction saturates at  $G_0$ , indicating that two unperturbed edge channels are now perfectly transmitted through the QPC over a large range of gate voltage (Fig. 4c,d).

Several other mechanisms might explain the 0.5 anomaly in QPCs or nanowires. These mechanisms include helical edge

reconstruction<sup>34</sup>, the formation of a Wigner crystal<sup>35</sup> or hyperfine interactions<sup>36</sup>. However, given the importance of the camel back in the valence band for our observation of the 0.5 anomaly, we believe that the mechanism presented here is the most plausible one. At the same time, we note (and discuss this more extensively in the Supplementary Information) it is possible to imagine another relevant mechanism, in particular the helical edge reconstruction proposed in ref.<sup>34</sup>, that shares many common ingredients with our mechanism—like strong spin–orbit coupling, electron–electron interactions and confinement. Hence, it is likely that the two mechanisms are related to each other.

### Online content

Any methods, additional references, Nature Research reporting summaries, source data, extended data, supplementary information, acknowledgements, peer review information; details of author contributions and competing interests; and statements of data and code availability are available at <https://doi.org/10.1038/s41567-019-0692-4>.

Received: 31 January 2019; Accepted: 13 September 2019;  
Published online: 28 October 2019

### References

- Kane, C. L. & Mele, E. J. Quantum spin Hall effect in graphene. *Phys. Rev. Lett.* **95**, 226801 (2005).
- Kane, C. L. & Mele, E. J.  $Z_2$  topological order and the quantum spin Hall effect. *Phys. Rev. Lett.* **95**, 146802 (2005).
- Bernevig, B. A., Hughes, T. L. & Zhang, S.-C. Quantum spin Hall effect and topological phase transition in HgTe quantum wells. *Science* **314**, 1757–1761 (2006).
- König, M. et al. Quantum spin Hall insulator state in HgTe quantum wells. *Science* **318**, 766–770 (2007).
- Knez, I., Du, R.-R. & Sullivan, G. Evidence for helical edge modes in inverted InAs/GaSb quantum wells. *Phys. Rev. Lett.* **107**, 136603 (2011).
- Wu, S. et al. Observation of the quantum spin Hall effect up to 100 kelvin in a monolayer crystal. *Science* **359**, 76–79 (2018).
- Reis, F. et al. Bismuthene on a SiC substrate: a candidate for a high-temperature quantum spin Hall material. *Science* **357**, 287–290 (2017).
- Roth, A. et al. Nonlocal transport in the quantum spin Hall state. *Science* **325**, 294–297 (2009).
- Brüne, C. et al. Spin polarization of the quantum spin Hall edge states. *Nat. Phys.* **8**, 486–491 (2012).
- Hou, C.-Y., Kim, E.-A. & Chamon, C. Corner junction as a probe of helical edge states. *Phys. Rev. Lett.* **102**, 076602 (2009).
- Ström, A. & Johannesson, H. Tunneling between edge states in a quantum spin Hall system. *Phys. Rev. Lett.* **102**, 096806 (2009).
- Teo, J. C. Y. & Kane, C. L. Critical behavior of a point contact in a quantum spin Hall insulator. *Phys. Rev. B* **79**, 235321 (2009).
- Tanaka, Y. & Nagaosa, N. Two interacting helical edge modes in quantum spin Hall systems. *Phys. Rev. Lett.* **103**, 166403 (2009).
- Dolcini, F. Full electrical control of charge and spin conductance through interferometry of edge states in topological insulators. *Phys. Rev. B* **83**, 165304 (2011).
- Krueckl, V. & Richter, K. Switching spin and charge between edge states in topological insulator constrictions. *Phys. Rev. Lett.* **107**, 086803 (2011).
- Zhang, L. B., Cheng, F., Zhai, F. & Chang, K. Electrical switching of the edge channel transport in HgTe quantum wells with an inverted band structure. *Phys. Rev. B* **83**, 081402 (2011).
- Orth, C. P., Strübi, G. & Schmidt, T. L. Point contacts and localization in generic helical liquids. *Phys. Rev. B* **88**, 165315 (2013).
- Sternativo, P. & Dolcini, F. Tunnel junction of helical edge states: determining and controlling spin-preserving and spin-flipping processes through transconductance. *Phys. Rev. B* **89**, 035415 (2014).
- Dolcini, F. Noise and current correlations in tunnel junctions of quantum spin Hall edge states. *Phys. Rev. B* **92**, 155421 (2015).
- Papaj, M., Cywiński, L., Wróbel, J. & Dietl, T. Conductance oscillations in quantum point contacts of InAs/GaSb heterostructures. *Phys. Rev. B* **93**, 195305 (2016).
- Micolich, A. P. What lurks below the last plateau: experimental studies of the  $0.7 \times 2e^2/h$  conductance anomaly in one-dimensional systems. *J. Phys. Condens. Matter* **23**, 443201 (2011).
- Bauer, F. et al. Microscopic origin of the ‘0.7-anomaly’ in quantum point contacts. *Nature* **501**, 73–78 (2013).
- Bendias, K. et al. High mobility HgTe microstructures for quantum spin Hall studies. *Nano Lett.* **18**, 4831–4836 (2018).
- Novik, E. G. et al. Band structure of semimagnetic Hg<sub>1-x</sub>Mn<sub>x</sub>Te quantum wells. *Phys. Rev. B* **72**, 035321 (2005).
- Skolasinski, R., Pikulin, D. I., Alicea, J. & Wimmer, M. Robust helical edge transport in quantum spin Hall quantum wells. *Phys. Rev. B* **98**, 201404 (2018).
- Schmidt, T. L., Rachel, S., von Oppen, F. & Glazman, L. I. Inelastic electron backscattering in a generic helical edge channel. *Phys. Rev. Lett.* **108**, 156402 (2012).
- Ortiz, L., Molina, R. A., Platero, G. & Lunde, A. M. Generic helical edge states due to Rashba spin–orbit coupling in a topological insulator. *Phys. Rev. B* **93**, 205431 (2016).
- Xie, H.-Y., Li, H., Chou, Y.-Z. & Foster, M. S. Topological protection from random Rashba spin–orbit backscattering: ballistic transport in a helical Luttinger liquid. *Phys. Rev. Lett.* **116**, 086603 (2016).
- Kharitonov, M., Geissler, F. & Trauzettel, B. Backscattering in a helical liquid induced by Rashba spin–orbit coupling and electron interactions: locality, symmetry and cutoff aspects. *Phys. Rev. B* **96**, 155134 (2017).
- Liu, C.-X., Budich, J. C., Recher, P. & Trauzettel, B. Charge–spin duality in nonequilibrium transport of helical liquids. *Phys. Rev. B* **83**, 035407 (2011).
- Giamarchi, T. *Quantum Physics in One Dimension* (International Series of Monographs on Physics, Oxford Univ. Press, 2003).
- Lunde, A. M., De Martino, A., Schulz, A., Egger, R. & Flensberg, K. Electron–electron interaction effects in quantum point contacts. *New J. Phys.* **11**, 023031 (2009).
- Sloggett, C., Milstein, A. & Sushkov, O. Correlated electron current and temperature dependence of the conductance of a quantum point contact. *Eur. Phys. J.* **61**, 427–432 (2008).
- Wang, J., Meir, Y. & Gefen, Y. Spontaneous breakdown of topological protection in two dimensions. *Phys. Rev. Lett.* **118**, 046801 (2017).
- Matveev, K. A. Conductance of a quantum wire in the Wigner-crystal regime. *Phys. Rev. Lett.* **92**, 106801 (2004).
- Hsu, C.-H., Stano, P., Klinovaja, J. & Loss, D. Effects of nuclear spins on the transport properties of the edge of two-dimensional topological insulators. *Phys. Rev. B* **97**, 125432 (2018).

**Publisher's note** Springer Nature remains neutral with regard to jurisdictional claims in published maps and institutional affiliations.

© The Author(s), under exclusive licence to Springer Nature Limited 2019

## Methods

**Device fabrication and measurement technique.** The QPCs were fabricated by a combination of electron-beam lithography and wet chemical etching on HgTe quantum well structures with a well width of either  $d_{\text{QW}} = 7.0$  nm or  $d_{\text{QW}} = 10.5$  nm. The layer stack was grown lattice matched on a  $\text{Cd}_{0.96}\text{Zn}_{0.04}\text{Te}$  substrate by molecular-beam epitaxy. The quantum well was sandwiched between  $\text{Hg}_{0.3}\text{Cd}_{0.7}\text{Te}$  barriers, and the bottom barrier was iodine-doped 70 nm below the quantum well (inset, Fig. 1b). The lithographic width of the QPCs ranged between 25 and 250 nm, and the length of the constriction was kept constant at  $L_{\text{QPC}} \approx 500$  nm (Fig. 1a). To control the charge carrier density within the QPC, a  $\text{HfO}_2$  insulator layer and a Ti/Au gate electrode were deposited to cover the centre of the QPC (Fig. 1a and schematic in Fig. 1b). Evaporated AuGe/Au layers were used to contact the quantum well electrically,  $\sim 80$   $\mu\text{m}$  away from the QPC.

Standard four-probe low-frequency lock-in techniques were used for the transport measurements at either 1.4 K or 25 mK base temperature.

## Data availability

The data that support the plots within this paper and other findings of this study are available from the corresponding author upon reasonable request.

## Acknowledgements

We thank E. Bocquillon, T. Borzenko, Y. Gefen, C. Gould, A. Currie, V. Hock, P. Leubner and Y. Meir for fruitful discussions. We acknowledge financial support by the DFG (SPP1666 and SFB1170 ‘ToCoTronics’), the ENB Graduate school on ‘Topological

Insulators’, the EU ERC-AG Program (project 4-TOPS) and the Würzburg–Dresden Cluster of Excellence on Complexity and Topology in Quantum Matter (EXC 2147, project ID 39085490). C.F. acknowledges support from the Studienstiftung des Deutschen Volkes.

## Author contributions

J.S. prepared the samples and performed the experiments. V.L.M. and P.S. contributed to implementation of the fabrication process, and S.S. and J.W. helped to carry out measurements. J.K. supervised the sample fabrication. J.W. guided the experiments. L.L. grew the material. W.B. provided the code for the band structure calculations. C.F., N.T.Z. and B.T. developed the theoretic model. H.B. and L.W.M. planned the project and design of the experiment. All authors participated in the analysis of the data, led by J.S. and J.W. All authors jointly wrote the manuscript.

## Competing interests

The authors declare no competing interests.

## Additional information

**Supplementary information** is available for this paper at <https://doi.org/10.1038/s41567-019-0692-4>.

**Correspondence and requests for materials** should be addressed to J.S., B.T. or L.W.M.

**Reprints and permissions information** is available at [www.nature.com/reprints](http://www.nature.com/reprints).